Journal Pre-proof

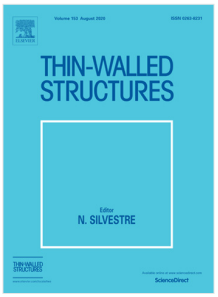

Topology-optimized multimaterial 4D-printed Fabry–Perot filter with enhanced thermal stability using two-photon polymerization

Johnny Moughames, Julio A. Iglesias Martínez, Gwenn Ulliac, Thibaut Sylvestre, Antoine Barbot, Jean-Claude André, H. Jerry Qi, Frédéric Demoly, Muamer Kadic

PII: S0263-8231(24)01339-9
DOI: https://doi.org/10.1016/j.tws.2024.112900
Reference: TWST 112900

To appear in: *Thin-Walled Structures*

Received date : 26 October 2024
Revised date : 8 December 2024
Accepted date : 30 December 2024

Please cite this article as: J. Moughames, J.A.I. Martínez, G. Ulliac et al., Topology-optimized multimaterial 4D-printed Fabry–Perot filter with enhanced thermal stability using two-photon polymerization, *Thin-Walled Structures* (2025), doi: https://doi.org/10.1016/j.tws.2024.112900.

Topology-optimized multimaterial 4D-printed Fabry-Perot filter with enhanced thermal stability using two-photon polymerization

Johnny Moughames[a], Julio A. Iglesias Martínez[b], Gwenn Ulliac[b], Thibaut Sylvestre[b], Antoine Barbot[b], Jean-Claude André[c], H. Jerry Qi[d], Frédéric Demoly[a,e], Muamer Kadic[b]

[a]*ICB UMR 6303 CNRS, Belfort-Montbeliard University of Technology, UTBM, Belfort, France*
[b]*FEMTO-ST UMR 6174 CNRS, Université de Franche-Comté, Besançon, France*
[c]*ICB UMR 6303 CNRS, Université de Bourgogne, UB, Dijon, France*
[d]*The George W. Woodruff School of Mechanical Engineering Georgia Institute of Technology Atlanta, GA 30332, USA*
[e]*Institut universitaire de France (IUF)*

Abstract

Tailoring material properties at the microscale is essential for advancing technologies, particularly in the field of 4D printing. The ability to manipulate thermal expansion is particularly critical for opto-mechanical systems, where precise deformation control is required. This paper introduces a novel approach that combines 4D printing with topology optimization to design and fabricate a multimaterial structure capable of mitigating undesired thermal expansion upon heat stimulation. This approach is applied to the development of a microfabricated Fabry-Perot filter as a robust alternative to directly printed cavity-based devices. Employing both approaches enables the determination of material distribution within the internal geometry of

Email address: johnny.moughames@utbm.fr (Johnny Moughames)

the structure, resulting to a temperature-insensitive response while maintaining optical performance. Using two-photon polymerization, the designed structure is 3D-printed with a combination of active and passive materials to achieve a controlled geometry. The final structure demonstrates a minimal change in dimensions under a temperature increase, confirming its ability to counteract thermal expansion effectively. This work showcases the potential of 4D printing and intelligent design strategies for developing devices at the microscale with precise thermal control.

Keywords: Topology optimization, 4D printing, Design, Thermal expansion, Fabry-Perot filter

1. Introduction

Computational materials design has emerged as a powerful tool for engineering structures with unprecedented properties. By precisely manipulating material composition and arrangement at the subwavelength scale, researchers can create materials with tailored functionalities [1, 2]. These advanced materials, often exhibiting properties beyond those found in nature [3, 4, 5], hold immense promise for revolutionizing fields such as electronics [6], optics [7, 8], energy, and biomedicine [9], among others. This approach combined with emerging technologies like 4D printing [10, 11], offers the potential to create dynamic systems with self-adapting properties [12, 13]. It involves the use of computer algorithms and simulations to optimize the geometric and material distribution within a structure, enabling the achievement of specific properties or functionalities [14]. For example, by modeling the behavior of

materials under different conditions, researchers can design materials with properties that can be dynamically adjusted in response to external stimuli [15, 16]. This capability enables the creation of innovative applications such as adaptive optics [17], tunable metamaterials [18], and multifunctional composites [19, 20]. Such advanced materials hold immense potential for revolutionizing the field of sensing [21]. By integrating computational design into sensor development, it is possible to create devices with enhanced sensitivity, selectivity, robustness, and improved operational stability [22].

A diverse range of optical and optomechanical devices have been successfully integrated onto optical fibers, using two-photon polymerization (TPP) technique [23, 24]. The direct accessibility of the guided light output from an optical fiber makes it an ideal platform for fabricating such elements at the fiber end face [25]. Fabry-Perot filters (FPF) can be used for measuring strain in structural components, detecting chemical species in gas or liquid environments, and monitoring biological processes. FPFs are also well-suited for temperature measurements due to their high sensitivity to changes in the optical path length, which can be induced by various physical mechanisms. Temperature variations can affect both the refractive index of the medium and the physical dimensions of the FPF cavity, leading to shifts in the resonant wavelengths [26]. A particularly promising application of FPF sensors lies in the field of biomedical sensing. By integrating FPF technology into minimally invasive devices, it is possible to monitor physiological parameters in real-time, enabling early disease and improved patient care. For example, FPFs could be used to measure blood pressure, glucose levels, and oxygen sat-

uration non-invasively [27, 28]. Additionally, FPFs can be incorporated into endoscopes and catheters to provide in situ sensing capabilities during surgical procedures [29, 30]. This can lead to more precise and efficient surgeries as well as reduce patient discomfort and recovery time. Fabry-Perot cavities, while offering high sensitivity and resolution, are highly sensitive to misalignment, with even slight deviations significantly affecting their quality factor (Q-factor). A high Q-factor, indicative of a narrow resonance linewidth, is crucial for achieving greater sensitivity and resolution. To mitigate the effects of misalignment, employing curved mirrors or increasing reflectivity can enhance tolerance. Furthermore, temperature variations can induce thermal expansion of the FPF cavity components, leading to changes in the optical path length and consequently shifting the resonant wavelength [31]. This, in turn can distort the sensor response and reduce measurement accuracy, especially when measuring physical parameters other than temperature. To address this, it is essential to implement temperature compensation techniques or utilize materials with minimal thermal expansion.

One common approach involves the use temperature compensation techniques, such as incorporating temperature-sensitive elements within the FPF cavity or utilizing sophisticated signal processing algorithms [30]. However, these methods often introduce additional complexity and cost to the system, and require a large number of data points to be collected and processed that can compromise the overall performance of the sensor. Another approach focuses on improving the stability of the FPF cavity by focusing on the development of materials with low coefficient of thermal expansion (CTE). Traditionally, materials such as silicon, fused silica, and certain crystalline

materials have been employed for fabricating FPF components due to their excellent optical properties and mechanical stability. However, these materials often exhibit relatively high CTE, limiting their suitability for high-precision sensing applications. To address these limitations and unlock the full potential of FPF sensors, there is a strong need for a new approach that goes beyond conventional compensation techniques and material selection.

Computational materials design offers a robust framework for optimizing the design of FPF components. By harnessing advanced computational techniques, such as topology optimization (TO), researchers can explore a vast design space and identify optimal material distributions and geometries to achieve desired performance and characteristics. Recent studies have demonstrated the potential of topology optimization in the design of 4D printed structures, where material distribution is optimized to achieve specific functional mechanical behaviors [32]. For instance, topology has been used to design soft actuators with enhanced stiffness and shape recovery properties [33].

Building upon these advancements, we propose a novel approach combining 4D computational design with two-photon polymerization to achieve highly thermally stable FPF. By employing topology optimization, we determine the optimal distribution of two materials with contrasting CTEs within the FPF cavity, while adhering to the constraints of TPP technique, including the minimum feature size (voxel), aspect ratio, and build orientation limitations. Departing from the traditional focus on mechanical performance in topology optimization for soft actuators, we leverage TO to optimize for ther-

mal expansion and contraction. This enables us to ensure minimal distortion of the FPF structure under varying temperature conditions.

Harnessing precise control over laser power (LP) during photopolymerization, we manipulate the photoresin crosslinking density, tailoring the thermal expansion properties of the resulting materials [12, 23, 24]. Building upon this capability, we fabricate uniaxial FPF components with a center wavelength of 1550 nm. These components exhibit reversible performance changes in response to temperature fluctuations, demonstrating their potential for various applications. To further expand functionality, we introduce biaxial configuration. By utilizing two materials with contrasting CTEs, this design enhances the thermal stability of the FPF, making it suitable for applications with significant temperature variations. To further expand functionality, we introduce biaxial configurations. By utilizing two materials with contrasting CTEs, this design insulates the FPF from temperature fluctuations, enabling the precise measurement of multiple physical parameters, such as force or pressure, unimpeded by thermal variations. This makes biaxial FPF components particularly well-suited for biosensing applications that require multi-dimensional detection, even in challenging thermal environments [31, 34].

2. Materials and methods

2.1. Design

To streamline the fabrication process and enhance the FPF's versatility, we developed an innovative clipping system that securely holds the optical fiber. As depicted in figure **1(a)**, this system consists of a cylindrical body with

curved plates that can be gently deformed to accommodate a standard single-mode fiber. A simple pushing mechanism ensures secure attachment, eliminating the need for intricate alignment procedures during fabrication, thereby streamlining the manufacturing process. Light injected into the fiber exits at its end and is emitted through a precisely defined optical aperture. This emitted light interacts with a parabolic micromirror positioned at the center of the filter cavity, as depicted in figure **1(b)**. The parabolic micromirror's curvature, optimized for both fabrication constraints and desired optical performance, ensures that incident light rays are precisely focused to a single point, significantly reducing aberrations such as spherical aberration and coma.

To further enhance the FPF's performance, we incorporate a gold layer (50 nm) onto the parabolic micromirror surface using electron-beam evaporation (EVA450 Thin layer coating, Alliance Concept, Paris, France). This reflective coating boosts the micromirror's reflectivity, leading to a notable increase in the intra-cavity optical power and consequent improvement in finesse. Additionally, to optimize the FPF's symmetry and light transmission within the fiber itself, we coat the fiber end face with a thinner gold layer ($10\ \text{nm} \pm 2\ \text{nm}$). This partially reflective coating establishes a balanced optical arrangement that enhances the quality of the resonant features leading to a narrower linewidth, higher extinction ratio, and ultimately, a substantially improved quality factor (Q).

An optical microscope of 20X is used to check the FPF/optical fiber assembly. Figure **1(c)** provides a visual representation of the device, showcasing

the fiber-clipping system and its integration within the microstructure. The polymer-based FPF's compact size, low power consumption, and sensitivity to external stimuli, make it a versatile platform for characterizing various physical properties. Its integration with optical fibers enables precise measurements even in remote or in field diagnostics applications. While its thermal expansion can be leveraged for precise temperature sensing by monitoring shifts in the free spectral range (FSR) of its cavity, characterizing other physical properties, such as force, can be challenging in environments with fluctuating temperatures. To accurately measure force in such conditions, it is essential to decouple the effects of temperature and force on the FPF's response.

In the following section, we will discuss strategies to address the thermal expansion of the polymer-based FPF structure and mitigate the effects of CTE variations on the device's performance.

2.2. CTE determination

To understand the polymer-based FPF's response to external stimuli, we must consider the underlying mechanical principles governing its behavior. The FPF's mechanical behavior can be described by the coupled elasticity and thermal expansion equations. These equations quantify the relationship between stress, strain, and displacement within the material. The equilibrium equations, given by:

$$\nabla \cdot \boldsymbol{\sigma} + \mathbf{b} = \mathbf{0} \tag{1}$$

where σ represents the internal stresses and $\mathbf{b}$ describes external forces within the FPF. The elastic polymer material is governed by the Hooke's law as

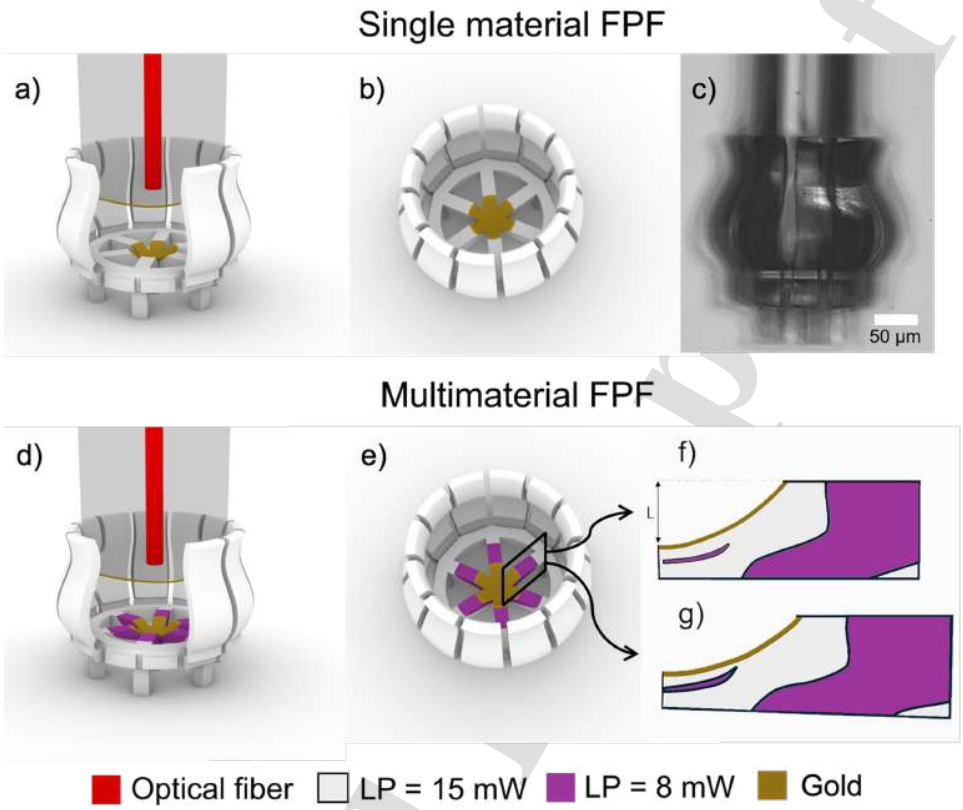

Figure 1: Design of single-material and multimaterial FPF. (a) 3D schematic representation of the FPF cavity attached to the end face of an optical fiber. (b) Top-view schematic representation of the FPF cavity's internal structure composed of a homogeneous material. (c) Optical microscope view of the FPF device, highlighting the seamless integration of the optical fiber within the 3D microstructure. (d) Similar to (a), but with the cavity interior featuring a multimaterial design achieved through TO using different laser powers (LPs): 8 and 15 mW. (e) Top view of the multimaterial cavity corresponding to (d). (f) and (g) schematically illustrate vertical cross-section through the FPF, as viewed from above in (e), revealing the continuous depthwise distribution of the two distinct polymers within the cavity. The two materials – depicted in tinted white and purple – represent polymers with lower and higher CTE, respectively. (f) Topology optimized (TO) 2D cavity at room temperature. (g) The multimaterial design mitigates thermal expansion within the cavity, ensuring that the focal point remains relatively stable across a wider temperature range.

follows:

$$\boldsymbol{\sigma} = \mathbf{C} : \boldsymbol{\varepsilon}_{\boldsymbol{elastic}} \tag{2}$$

where σ is the stress, ε is the strain, and $\mathbf{C}$ the elasticity tensor. This constitutive equation allows us to quantitatively analyze the mechanical behavior of the polymer material under various loading conditions.

To understand the relationship between the displacement of material points u and the total strain ϵ_{total}, we use the strain-displacement relation:

$$\boldsymbol{\varepsilon}_{\text{total}} = \frac{1}{2}\left(\nabla \mathbf{u} + (\nabla \mathbf{u})^T\right) \tag{3}$$

This equation defines the total strain ϵ_{total}. To separate the elastic strain $\epsilon_{elastic}$ from the total strain, we consider the effect of thermal expansion, which is represented by the thermal strain equation:

$$\boldsymbol{\varepsilon}_{\text{thermal}} = \alpha \Delta T \boldsymbol{I} \tag{4}$$

Here, α is the coefficient of thermal expansion (CTE), ΔT is the temperature change, and $\boldsymbol{I}$ is the identity matrix.

The elastic strain $\epsilon_{elastic}$ is then given by:

$$\boldsymbol{\varepsilon}_{\text{elastic}} = \boldsymbol{\varepsilon}_{\text{total}} - \boldsymbol{\varepsilon}_{\text{thermal}} \tag{5}$$

By carefully analyzing the FPF's response to external stimuli and considering these mechanical principles, we can gain valuable insights into its behavior and optimize its performance for various applications.

2.3. Material optimization

The design of an FPF that can operate reliably across a wide range of temperature conditions, while maintaining good optical performance in terms of

reflection efficiency, aberration minimization, and reduced sensitivity to external influences, requires the establishment of an appropriate optimization problem. Here, the main objective function is described as follows:

$$\delta = \min\left(\frac{\int \overline{\omega}(\rho_1)dl}{L}\right) \tag{6}$$

This objective function aims to minimize the average optical path length variation $\overline{\omega}$ within the filter due to temperature variation. The normalized optical path length variation (δ) is calculated as the ratio of the average optical path length variation $\overline{\omega}(\rho_1)$ over the entire optical path length (dl) to the total optical length (L). The integration is performed over the relevant region of the structure, with ρ_1 representing the material distribution ($\rho_1 = 0$ for material 1, $\rho_1 = 1$ for material 2).

To minimize δ, we must carefully engineer the FPF dimensions, micromirror reflectivities, and materials properties to mitigate the central expansion of the micromirror, reduce stress-induced birefringence, and ensure the optical path length remains relatively constant over a wide temperature range.

The micromirror's reflective surface is meticulously defined according to the following equation,

$$z = -\frac{1}{4f}s^2 + f \tag{7}$$

where, z represents the height of a point on the parabola, s represents the horizontal distance from the axis of symmetry of the micromirror to any point on the parabola, and f is the focal length of the parabola.

We employ a density-based topology optimization model to determine the material distribution within the designated design domain. We define a de-

sign field, ρ_1, that can continuously vary between 0 and 1 to interpolate between the low and the high CTE material in the design domain, as follows,

$$0 \leq \rho_1 \leq 1 \tag{8}$$

To mitigate numerical instabilities and ensure a smooth transition between material phases, a smoothing step was applied to the design field. This involved filtering the design variable, $\overline{\rho_1}$, using Helmholtz filter,

$$\overline{\rho_1} = R_{\min}^2 \nabla^2 \overline{\rho_1} + \rho_1 \tag{9}$$

with a smoothing radius, $R_{\min}$ of 800 nm. This process aid in limiting the appearance of small design feature and prevents a mesh-dependent solution. To sharpen the gray areas in the design field and facilitate a clear distinction between materials with different thermal expansion coefficients, a hyperbolic tangent function was employed. This function is defined as,

$$T_h = \frac{\tanh(\beta(\overline{\rho_1} - \theta_\beta)) + \tanh(\beta\theta_\beta)}{\tanh(\beta(1 - \theta_\beta)) + \tanh(\beta\theta_\beta)} \tag{10}$$

that transforms the design field towards binary values close to 0 or 1 to realize realistic designs of either low or high thermal expansion material. The parameter θ_β defines the threshold in the function, whereas the parameter β controls the threshold sharpness. We apply the threshold operation (equation (10)) on the smoothed design field with the threshold being at the center value $\theta_\beta = 0.5$:

$$\widetilde{\theta} = T_h(\overline{\rho_1}, \beta, \theta_\beta) \tag{11}$$

We progressively double the threshold sharpness starting from 1 and ending at 12 using a continuation approach to achieve a binary-inspired design. We use the thresholded design field, $\widetilde{\theta}$, to interpolate into a thermal-expansion distribution in the design domain with a linear material interpolation between the low and high CTE materials,

$$\alpha = -\widetilde{\theta}(\alpha_2 - \alpha_1) + \alpha_1 \tag{12}$$

The optimized multimaterial distribution for the micromirror and its surrounding is illustrated in figure **1(d)**. Figure **1(e)** depicts a top view of the FPF biaxial configuration, highlighting the six identical sections around the parabolic micromirror. Figure **1(f)** presents a 2D cross-section of one of these sections, focusing on the depth distribution of the materials. Figure **1(g)** demonstrates the thermal expansion of the topology-optimized multimaterial structure when subjected to a temperature difference of 45°C (from 30 °C to 75 °C). It also illustrates how the materials expand while maintaining the focal distance of the parabolic micromirror. Notably, the central region of the mirror exhibits near-zero displacement, ensuring consistent optical performance across a range of temperatures.

By carefully tuning the thresholding parameters, such as the sharpness parameter β and the threshold value θ_β, we were able to achieve precise control over the material distribution. This enabled the creation of a well-defined and manufacturable FPF design, culminating in the specific geometry of the micromirror depicted in figure **2(a)**. The sharpness parameter β allowed us to balance the need for sharp material interfaces with the requirements of manufacturability. The threshold value θ_β determined the optimal distribution of the two materials, ensuring that the desired thermal expansion

properties were achieved, which is crucial for maintaining the micromirror's shape and optical performance under varying temperature conditions. The geometry of the micromirror depicted in figure **2(a)** shows a vertical half-cut of the 3D structure. The design size domain of the micromirror is 50 µm in diameter and 20 µm in depth, operating at a central wavelength of 1550 nm.

3. Fabrication of the FPF structure

The FPF is comprised with two primary components: a single-mode optical fiber (SMF) and a 3D microstructure part. The SMF, conforming to the G.652.D standard with a 9 μm core and 125 μm silica cladding (ITU-T [G.652]) [35] is used to couple with the 3D microstructure. The 3D microstructure consists of a parabolic micromirror with nearly 100% reflectance. To compensate for thermal-induced changes in focal distance, the 3D microstructure was fabricated using two materials with different CTEs. The 3D microstructure was fabricated using Nanoscribe GT2 printer (Karlsruhe, Germany) laser-based TPP system operating at 780 nm. IP-S, a commercial photoresin with high refractive index [36], is used as the printing material. By optimizing the laser power and applying the results of the topology optimization study discussed in section 2, we successfully distributed the high-CTE and low-CTE materials around the parabolic micromirror.

To achieve optimal FPF performance, we conducted experiments to determine the ideal power for printing the micromirror. By fabricating multiple micromirrors at varying power levels, we were able to observe the impact of different power on the resulting structures. Figure **2(b)** illustrates how high powers (above 16 mW) can lead to damage and deformation, while low power (below 10 mW) may lead to incomplete polymerization. By carefully

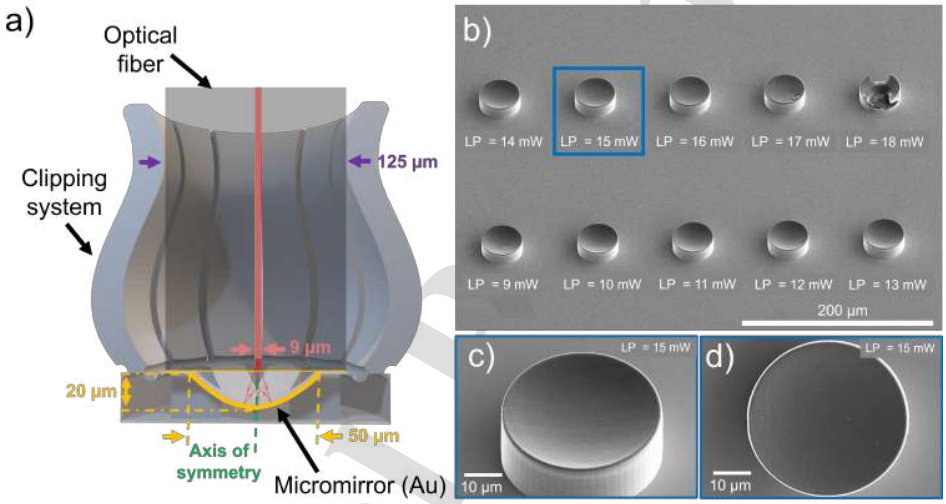

Figure 2: Fabrication of high-resolution micromirrors using multiparameter optimization. (a) Illustration of the FPF's operating principle. (b) SEM images of fabricated micromirrors printed with varying laser powers aiming to identify the optimal laser power. (c) Tilted view revealing fine features and surface smoothness of the micromirror for efficient reflection and minimal scattering. (d) Top view demonstrating overall uniformity of the micromirror's reflective surface for consistent light coupling.

selecting a power of 15 mW, we were able to achieve a balance between structural integrity and optical performance. Figures **2(c)** and **2(d)** depict SEM tilted view and top view of the micromirror, respectively, with the best combination of smooth surface and minimal defects. Based on the same study, we choose the LP= 8 mW to print the high CTE material. Figure **3(a)** shows the SEM top view image of the two material distribution into the 3D structure. The high contrasted micromirror part with light gold color at the center represents the low CTE material, while the light purple colored parts surrounding the mirror represent the high CTE material.

To further enhance the FPF's Q-factor, we employed precise coating techniques using Leica ACE600 sputter coater (Wetzlar, Germany) to increase mirror reflectivity. Prior to coating, the fiber's end face was precision-cleaved to create a flat surface, ensuring optimal optical coupling. A thin gold layer of $10nm$ was then deposited onto the cleaved surface. This gold layer served as both a protective coating and semi-reflective mirror, reflecting a portion of the light back into the cavity. To enhance the reflectivity of the 3D structure micromirror we deposited a 50 nm gold coating. This combination significantly increased the reflectivity of both surfaces, resulting in a more confined optical field within the cavity.

To improve fabrication efficiency, we utilized different hatching distances to print voxels in the horizontal directions for the micromirror and the mechanical parts [37, 38]. A smaller hatching distance of 100 nm is employed for the micromirror to avoid surface roughness, while a larger hatching distance of 800 nm is used for mechanical areas that did not interact with light. This approach allows for faster fabrication times without compromising the FPF's

performance.

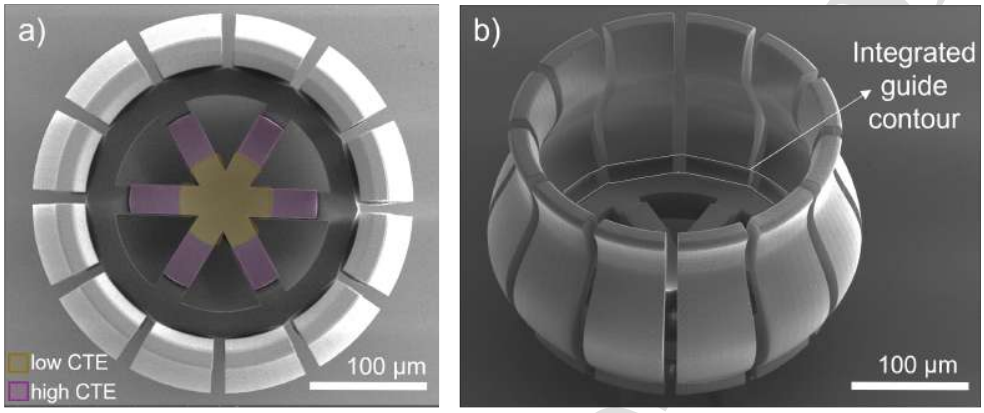

Figure 3: SEM images of the multimaterial FPF cavity. (a) Top view SEM image of the FPF cavity, highlighting the micromirror region (tinted gold) and the surrounding regions (tinted purple). The micromirror, fabricated with high laser power, exhibits a lower CTE compared to the surrounding regions, which were fabricated a lower laser power. This differential CTE enables precise control over the thermal expansion of the structure. (b) Tilted-view SEM image of the FPF cavity, showcasing the integrated waveguide contour. This feature ensures precise fiber alignment, enhances vibration damping, and provides structural support during fiber insertion.

To ensure the FPF's structural integrity and optical alignment, we implemented a series of supporting structures surrounding the micromirror. Figure **3(b)** presents a 45° tilted view of the clipping system, a critical component for coupling the FPF to the optical fiber. This system incorporates multiple, stacked polymer shelves designed to be mechanically compliant and deformable. This compliance facilitates the gentle insertion of optical fibers without inducing damage to either the fiber or the FPF's sensitive components, including the micromirror. We improved micromirror alignment by guiding the optical fiber through the clipping system and then integrating a 125 μm diameter guide contour with a 10 μm thickness to hold the fiber in a straight position. This precise alignment ensures that the light beam travels

parallel to the optical axis of the FPF. By systematically addressing these factors, we significantly increase the Q-factor of our FPF, demonstrating the importance of optimizing these parameters for achieving high-performance optical filters.

4. Experimental measurements and observations

The optical setup employed in the characterization experiment of the FPF is composed of a widely wavelength-tunable fiber laser source from 1440 nm to 1640 nm, a 50/50 fiber coupler (FC) is used to isolate the reflection from the FPF and an optical spectral analyser (OSA, Agilent 86142B). The wavelength-tunable laser was connected to the first port of the FC, while the FPF was connected to the second port. The third port (output port) of the FC is connected to the input port of the OSA to measure the FPF spectral function. The device was enclosed within a temperature-controlled chamber (Linkam THMS600, Waterbeach, Cambridgeshire, United Kingdom), equipped with an optical window. This chamber maintained a stable temperature range of 30 to 75°C, with a fluctuation of ±1°C. Once the chamber reaches the desired temperature, the laser is tuned on and sweep across a large bandwidth ranging from 1460 to 1600 nm. The laser exhibits a wavelength-dependent power output, which was subtracted from each measurement. Each reading then presented a voltage proportional to the reflected power across the spectrum introduced by the tunable laser.

Subsequently, the measured FPF spectra are normalized and plot in logarithmic scale in figures **4(a)** and **5(a)**. These figures show the experimental results for temperatures ranging from T= 30°C to 75°C in increments of 1°C for the single and multimaterial polymer 3D microstructure, respectively. An

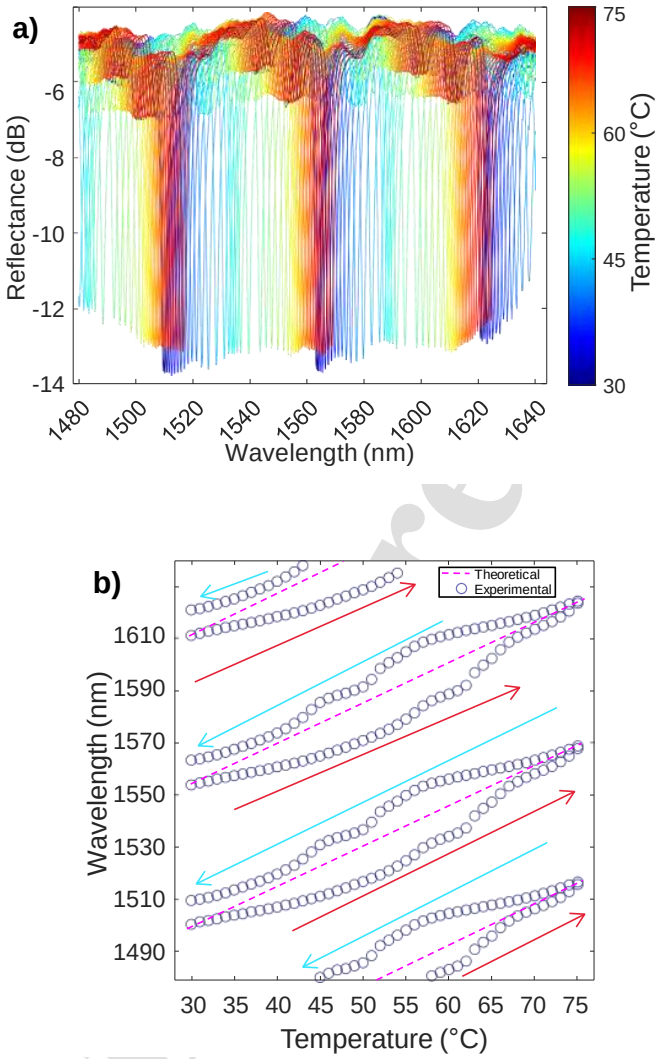

Figure 4: **Characterization of the single polymer FPF**. (a) Plot showing the spectral response (reflectance vs. wavelength) of the single-material FPF cavity at various temperatures. The observed shifts in the resonant peaks with temperature variations are attributed to thermal expansion of the cavity, altering its effective length. (b) Plot illustrating the hysteresis behavior of the single-material cavity during temperature cycling. Blue circles represent measured wavelengths at each temperature. The pink dashed line indicates the expected theoretical wavelength shift based on thermal expansion of the polymer.

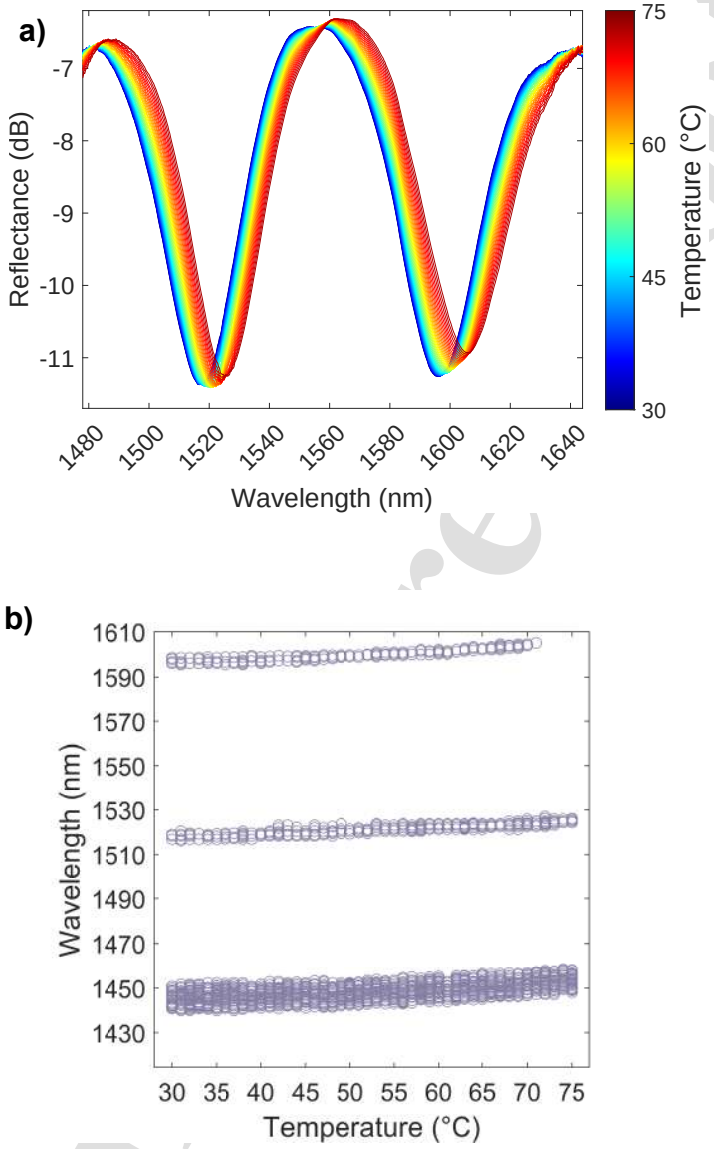

Figure 5: **Characterization of the multimaterial polymer FPF with 4D topological optimization.** (a) Plot illustrating the spectral response (reflectance vs. wavelength) of the multimaterial FPF device with 4D optimized topology at different temperatures. The 4D optimized material distribution enables precise control over the device's thermal expansion, resulting in minimal shifts in the resonant peaks. (b) Plot illustrating the behavior of the multimaterial FPF device with 4D optimized topology during temperature cycling. Blue circles represent measured wavelengths at each temperature. The 4D optimized material distribution effectively compensates for thermal expansion, leading to negligible shifts in the resonant peaks.

Airy distribution is overlaid on the plots for visualization purposes only. The central wavelengths of the dip resonances were experimentally determined and plotted as blue circles in figures **4(b)** and **5(b)** for each temperature. The dashed line in figure **4(b)** represents the theoretically predicted shift in resonant wavelength due to thermal effects, calculated using the following equation:

$$\Delta\lambda = \frac{(\alpha L + \Delta n L)}{Q} \tag{13}$$

where $\Delta\lambda$ is the change in resonant wavelength (nm), α is the CTE. As shown in figure **4(b)**, the observed shift in resonance follows a linear trend, aligning with the predictions of equation **13**. The experimental data closely tracks the theoretical curve, demonstrating good agreement between theory and experiment. A significant degree of hysteresis between the heating and cooling cycles of the device's temperature. We attribute this to the micromirror's settling after initial expansion into the clearance between the 3D microstructure and the OF. This would explain the consistent offset between the two measurements. This hysteresis is significantly reduced in the multimaterial FPF device due to effective material compensation.

In summary, the single-material FPF device exhibits a linear thermal response, closely aligning with theoretical predictions. Nevertheless, the device suffers from significant hysteresis and thermal expansion effects due to the use of a single material with a uniform coefficient of thermal expansion. In contrast, the multimaterial FPF device, with its optimized material distribution, effectively mitigates these issues, demonstrating improved thermal stability and performance. Figure 5(b) clearly demonstrates that the

wavelength-dependent temperature variation is significantly reduced when compared to the single-material FPF. Specifically, the temperarure coefficient is lowered from 1.48 nm/°C depicted from figure 4 down to 0.09 nm/°C for the second resonance. This reduction is a crucial result, as it highlights the effectiveness of the multimaterial FPF in minimizing thermal sensitivity, which is important for enhancing the stability and performance of devices operating under varying temperature conditions. Furthermore, as observed in figure 5(b), the temperature hysteresis has nearly disappeared when using the multimaterial FPF.

5. Conclusion

In this paper, we demonstrated a novel approach showcasing the fabrication of Fabry-Perot filters using a single-step multimaterial two-photon polymerization. This direct printing technique enables the creation of high-quality optical surfaces within the 3D microstructures. Furthermore, the unique design flexibility afforded by our clipping system on an optical fiber tip allows for the straightforward integration of high-reflectivity coatings, potentially enhancing the cavity's Q-factor. By leveraging density-based topology optimization, we have demonstrated a significant reduction in temperature-induced performance variations. This optimized design, realized through a single-step TPP process, makes these cavities particularly well-suited for embedded applications where precise optical performance is critical, regardless of the surrounding temperature. This opens up new possibilities for their integration into various systems, including biological sensors and other sensitive devices.

Acknowledgments

We acknowledge Marina Raschetti for providing the SEM images, and Jean-Charles Beugnot and Maxime Romanet for their assistance with fiber processing. This work has been achieved in the frame of the EIPHI Graduate school (contract "ANR-17-EURE-0002"), ANR PNanoBot (ANR-21-CE33-0015), ANR OPTOBOTS (ANR-21-CE33-0003), ISITE-BFC 4D-META (contract ANR-15-IDEX-0003), and the french RENATECH network and its FEMTO-ST technological facility (MIMENTO).

References

[1] G. Sossou, F. Demoly, H. Belkebir, H. J. Qi, S. Gomes, and G. Montavon, Materials & Design **181**, 108074 (2019).

[2] D. Athinarayanarao, R. Prod'hon, D. Chamoret, H. J. Qi, M. Bodaghi, J.-C. André, and F. Demoly, npj Computational Materials **9**, 1 (2023).

[3] J. A. Iglesias Martínez, J. Moughames, G. Ulliac, M. Kadic, and V. Laude, Appl. Phys. Lett. **118**, 063507 (2021).

[4] M. Kadic, G. Dupont, S. Enoch, and S. Guenneau, Phys. Rev. A **90**, 043812 (2014).

[5] M. Kadic, T. Bückmann, R. Schittny, and M. Wegener, Rep. Prog. Phys. **76**, 126501 (2013).

[6] X. Kuang, D. J. Roach, C. M. Hamel, K. Yu, and H. J. Qi, Multifunctional Materials **3**, 032002 (2020).

[7] J. Moughames, S. Jradi, T. Chan, S. Akil, Y. Battie, A. E. Naciri, Z. Herro, S. Guenneau, S. Enoch, L. Joly, *et al.*, Scientific reports **6**, 33627 (2016).

[8] J. Moughames, X. Porte, M. Thiel, G. Ulliac, L. Larger, M. Jacquot, M. Kadic, and D. Brunner, Optica **7**, 640 (2020).

[9] P. H. Kao, S. R. Lammers, L. Tian, K. Hunter, K. R. Stenmark, R. Shandas, and H. J. Qi, (2011).

[10] F. Demoly and J.-C. Andre, *4D Printing, Volume 2: Between Science and Technology* (John Wiley & Sons, 2022).

[11] F. Demoly and J.-C. André, Applied Sciences **14**, 5669 (2024).

[12] Q. Ji, J. Moughames, X. Chen, G. Fang, J. J. Huaroto, V. Laude, J. A. I. Martínez, G. Ulliac, C. Clévy, P. Lutz, *et al.*, Communications Materials **2**, 93 (2021).

[13] M. Mohammadi, A. Z. Kouzani, M. Bodaghi, J. Long, S. Y. Khoo, Y. Xiang, and A. Zolfagharian, "bibfield journal "bibinfo journal Robotics and Computer-Integrated Manufacturing" "textbf "bibinfo volume 85," "bibinfo pages 102636 ("bibinfo year 2024).

[14] X. Chen, J. Moughames, Q. Ji, J. A. I. Martínez, H. Tan, G. Ulliac, V. Laude, and M. Kadic, J. Mech. Phys. Solids , 105057 (2022).

[15] M. Kadic, M. Wegener, A. Nicolet, F. Zolla, S. Guenneau, and A. Diatta, arXiv preprint arXiv:1906.02797 (2019).

[16] X. Chen, J. Moughames, Q. Ji, I. Martínez, H. Tan, S. Adrar, N. Laforge, J. Cote, S. Euphrasie, G. Ulliac, *et al.*, Extreme Mech. Lett. **41**, 101048 (2020).

[17] X. Porte, N. Dinc, J. Moughames, G. Panusa, C. Juliano, M. Kadic, C. Moser, D. Brunner, and D. Psaltis, Optica **8**, 1281 (2021).

[18] X. Chen, N. Laforge, Q. Ji, H. Tan, J. Liang, G. Ulliac, J. Moughames, S. Adrar, V. Laude, and M. Kadic, Comptes Rendus. Physique , 1 (2021).

[19] F. Demoly, M. L. Dunn, K. L. Wood, H. J. Qi, and J.-C. André, Materials & Design **212**, 110193 (2021).

[20] H. Y. Jeong, E. Lee, S.-C. An, Y. Lim, and Y. C. Jun, Nanophotonics **9**, 1139 (2020).

[21] X. Tan, J. A. I. Martínez, G. Ulliac, B. Wang, L. Wu, J. Moughames, M. Raschetti, V. Laude, and M. Kadic, Small **18**, 2202128 (2022).

[22] N. Semenova, J. Moughames, X. Porte, M. Kadic, L. Larger, and D. Brunner, in *AI and Optical Data Sciences II*, Vol. 11703 (SPIE, 2021) p. 117030I.

[23] J. B. Mueller, J. Fischer, F. Mayer, M. Kadic, and M. Wegener, Adv. Mater. **26**, 6566 (2014).

[24] L. Yang, A. Münchinger, M. Kadic, V. Hahn, F. Mayer, E. Blasco, C. Barner-Kowollik, and M. Wegener, Adv. Opt. Mater. **7**, 1901040 (2019).

[25] T. Gissibl, S. Thiele, A. Herkommer, and H. Giessen, Nature photonics **10**, 554 (2016).

[26] Z. S. Alshaikhli, Applied Physics A **130**, 127 (2024).

[27] I. Martincek and G. Tarjanyiova, IEEE Sensors Journal (2024).

[28] R. Yin, Y. Yang, L. Hou, H. Wei, H. Zhang, and W. Zhang, Photonics Research **12**, 2474 (2024).

[29] Z. Mo, W. Xu, and N. Broderick, in *2015 6th International Conference on Automation, Robotics and Applications (ICARA)* (IEEE, 2015) pp. 376–380.

[30] Y. Deng, T. Yang, B. Lou, K. Yu, G. Song, and S. Dai, Sensors and Actuators A: Physical **342**, 113645 (2022).

[31] Z. Mo and W. Xu, IEEE Sensors Journal **16**, 8936 (2016).

[32] A. Zolfagharian, M. Denk, M. Bodaghi, A. Z. Kouzani, and A. Kaynak, Acta Mechanica Solida Sinica **33**, 418 (2020).

[33] A. Zolfagharian, M. Denk, A. Z. Kouzani, M. Bodaghi, S. Nahavandi, and A. Kaynak, International Journal of Bioprinting **6** (2020).

[34] A. Haleem, M. Javaid, R. P. Singh, R. Suman, and S. Rab, Sensors International **2**, 100100 (2021).

[35] G. ITU-T, International Telecommunication Union, Geneva, Switzerland (2016).

[36] M. Schmid, D. Ludescher, and H. Giessen, Optical Materials Express **9**, 4564 (2019).

[37] J. Moughames, X. Porte, L. Larger, M. Jacquot, M. Kadic, and D. Brunner, Opt. Mater. Express **10**, 2952 (2020).

[38] A. Grabulosa, J. Moughames, X. Porte, and D. Brunner, Nanophotonics **11**, 1591 (2022).

Highlights

- Multi-physical 4D printed mechanical metamaterial
- Topological designed 4D metamaterial for temperature compensation
- 3D printed device combining optical and mechanical metamaterials

Declaration of Interest Statement

The authors declare no conflict of interest.